ORNL/CP-94929

RECEIVED
NOV 04 1997
OSTI

CONF-9709120--

Weldability and Microstructure Development in Nickel-Base Superalloys

S. A. David, S. S. Babu, and J. M. Vitek

Metals and Ceramic Division, Oak Ridge National Laboratory,
Oak Ridge, TN 37831, USA

Paper to be submitted for the Proceedings of the Conference on "Numerical Analysis of Weldability - V,," Graz, Austria, 1997

"The submitted manuscript has been authored by a contractor of the U S. Government under contract NO. DE-AC05-96OR22464. Accordingly, the U.S. Government retains a nonexclusive, royalty-free license to publish or reproduce the published form of this contribution, or allow others to do so, for U.S. Government purposes."

DISTRIBUTION OF THIS DOCUMENT IS UNLIMITED

MASTER

Weldability and Microstructure Development in Nickel-Base Superalloys

S. A. David, S. S. Babu, and J. M. Vitek

Metals and Ceramics Division, Oak Ridge National Laboratory,
Oak Ridge, TN 37831, USA

Abstract

The integrity of nickel-base superalloy single-crystal welds depends on the weld cracking tendency, weld metal dendrite selection process, stray crystal formation, and macro- and microstructure development. These phenomena have been investigated in commercial nickel-base superalloy single crystal welds. During electron beam and laser beam welding, transverse and longitudinal weld cracking occurred. However, the weld cracking tendency was reduced with preheating. Most of the dendritic growth pattern development in these welds can be explained by a geometric model. However, the welds also contained misoriented stray crystals, which were frequently associated with weld cracks. The formation of stray crystals was related to thermal and constitutional supercooling effects. Fine-scale elemental partitioning between γ and γ' phase was measured with atom-probe field-ion microscopy. Marked differences in partitioning characteristics in two welds were observed and are related to differences in cooling rates. In this paper, the modeling tools available to describe the above are reviewed.

Introduction

Because of their excellent high temperature creep resistant properties, nickel-base superalloys are commonly used in land-based and aerospace turbines.[1] To meet the ever-increasing demand for higher operating temperatures, both processing methods and alloy designs have been improved to produce two major microstructural features: (1) reduced grain boundaries and (2) higher stability and volume fractions of γ' phases. The grain boundaries are reduced or eliminated by resorting to directional solidification or single crystals. The stability and volume fractions of γ' phases are modified by careful alloy modifications and heat treatments.[2] The high replacement costs of these components have necessitated the repair of aircraft gas-turbine engine components, and welding is considered a desirable and economical alternative.[3] However, the poor strength and poor weldability of these alloys have remained critical issues.

Welding involves melting and solidification and raises the following issues. (1) Weld cracking is common in nickel-base superalloys. During weld cooling, thermal stresses develop and may lead to weld cracking. The stresses depend on the welding parameters and the joint design. The weld cracking also depends on the microstructural parameters, such as the presence of low-melting-point eutectics at the solidifying dendritic boundary. These low-melting eutectics may exist as a liquid film at temperatures well below the equilibrium solidus and reduce the grain boundary cohesion.[4] (2) During welding of single crystals, the welded component may loose its single-crystallinity or develop complex dendritic patterns during welding. (3) In addition, the γ' precipitation in the weld metal region occurs during rapid cooling conditions and is expected to be different from that of the base metal. This paper discusses various results related to the preceding issues in commercial nickel-base superalloy single-crystals.

Experimental Details

Alloys

Two commercial single-crystal alloys, PWA-1480 and CMSX-4, were investigated. Their compositions are given in Table 1. In addition, an experimental single-crystal alloy similar in composition to that of IN-738, referred to as M738, was used in the weld crack monitoring investigations.

Welding Process and Parameters

Autogeneous electron beam and laser beam welds of the PWA-1480 alloy were made on single-crystal discs of 1.5 cm in diameter and 0.3 cm in thickness. The surface of the discs of the PWA-1480 alloys were (001) and (110) planes. The welds were made in controlled crystallographic directions, [110] and [100]. The electron beam (EB) welds were made in a horizontal position with a 15-kW Leybold Heraeus EB welding machine with a 100-kV accelerating voltage, 3 to 13 mA beam current, and welding speeds of 4.2 to 42 mm s^{-1}. Some EB welds were made with 500 °C preheating. In the case of the CMSX-4 alloys, small sections (2 to 3 mm thick) were cut from the single-crystal castings. Laser welds were made using a pulsed Nd:YAG laser capable of delivering an average power of 400 W. The pulse rate ranged from 20 to 200 s^{-1}, and the welding speed ranged from 2 to 13 mm s^{-1}. Only laser welds were made on the CMSX-4 alloys.

Weld Crack Monitoring

To monitor weld cracking in real time, a "vision-system" was used.[5] In this experiment, a particular location along the weld centerline was illuminated by stroboscopic light. This allows a charge-coupled device (CCD) camera to record the weld pool formation and subsequent cracking behavior even in the presence of a bright arc. The location of observation was chosen based on repeated experimental trials. The weld formation and subsequent cracking at this location were was recorded with the camera. Welds were made on an experimental M738 alloy using the GTAW welding process. To promote weld cracking, the weld was restrained in a SigmaJig[6] fixture (see Fig. 1). The GTA welding parameters were as follows: welding current was 75 A, welding speed was 12.7 mm s^{-1} and the prestress was 68 MPa.

Microstructural Characterization

Detailed microstructural analysis was performed using conventional optical and electron microscopy techniques. In addition, an atom-probe field-ion microscope[7] was used to characterize the partitioning and possible segregation at the γ/γ' interfaces. The samples were imaged at a temperature range of 50 to 60 K with a residual neon gas pressure of 3×10^{-7} Pa and a pulse fraction of 20% in the atom-probe.

Weld Cracking

Most nickel-base superalloys are prone to weld solidification cracking.[3] It is known that weld solidification cracking is accentuated by two factors: stress (thermal and physical restraints in the joint) and alloy dependent features (low-melting eutectic film, large solidification temperature range, and grain structure). For example, a combination of the presence of low-melting-point eutectic films and large thermal stresses may lead to weld cracking.[8] Both of these factors may be affected by the welding process parameters. In the following section, the dynamics of weld cracking and the effects of welding process parameters on cracking tendency are discussed.

Direct Observation of Weld Cracking

It is often very difficult to study the onset of weld cracking in real welds because of the presence of the bright arc. However, the vision-system apparatus described above allows one to monitor the formation of the weld pool and the subsequent cracking with the use of a special CCD camera and stroboscopic lighting of the weld surface. Series of surface images at a particular location on a M738 alloy sample were recorded and is presented in Fig. 2. The figure shows the arc passing under the camera, the solidified weld pool, the onset of transverse weld cracking, and the completely cracked weld. The time interval for each stage was also recorded. The results showed that the weld pool solidification was completed at 1.19 s. This was deduced by observing the trailing edge of the weld pool. The weld cracking started at 2.30 s. This indicates that the weld cracking, investigated in this study, is subsolidus in nature. It is known that M738 alloys have a large solidification range and tend to form low melting eutectics. Moreover, the welds were made with preapplied tensile stress.

Note that cracking started much after the completion of the weld pool solidification (at a lower temperature) and that the cracking did not start at the trailing edge of the weld pool. This suggests that even though there are large fractions of liquid in the trailing edge of the weld pool, there must not be any large tensile stresses at this location to initiate rupture. Instead, transverse cracking occurs after solidification. Therefore, there must be large longitudinal stresses and weak microstructural features at this location. The welding experiments also revealed longitudinal cracks in other parts of the welds. Such cracking tendencies should be related to the transient stress states of the weldment as well as factors related to microstructure development.[8]

Weld Cracking in Single-Crystal Alloys

The weld cracking tendency was investigated after welding in various weld directions in PWA-1480 single crystal samples. These investigations were performed with EB and pulsed laser-beam welding processes.[3] In these experiments, most of the welds cracked. The cracks were both longitudinal and transverse. Figure 3 shows the extent of cracking in a typical EB weld. The micrographs also indicate that the cracks were associated with regions that contain stray crystals (dendritic-growth patterns that were not among the six <100> variants of the base material). These regions, containing stray crystals, are marked by arrows. The dendritic-growth patterns and the formation of stray crystals are discussed later. Only in a few cases were acceptable welds produced without cracking. The effects of welding speed and preheating were also studied. In the case of pulsed laser-beam welds, the effect of the pulsing rate was also investigated. The details of macrostructure and microstructure can be seen in the reference 3 and 9. The results are in Tables 2 through 4 and can be summarized as follows:

(1) The welding direction had no effect on the weld cracking. However, there were changes in the solidification dendrite patterns.[3,9]

(2) The welding speed affected the weld pool shape and size.[3,9]

(3) Preheating to 500°C and low welding speeds reduced the cracking tendency. However, preheating at high welding speeds still led to weld cracking.[3]

(4) In the case of laser welding, the pulse rate did not change the cracking tendency. High laser pulse rates, for a given welding speed, led to the formation of a continuous weld. In contrast, small pulse rates lead to the formation of overlapping spot welds. Crack-free welds were obtained only at slow welding speeds (2.1 to 4.2 mm s^{-1}).[3]

In summary, successful crack-free welds were obtained at low welding speeds and with preheating to 500°C. It is obvious that slow welding speeds and preheating, for a given welding process, will reduce the weld metal cooling rate. The reduced weld cooling rates may lead to large extent of solute partitioning in the liquid and may promote the formation of large amounts of low-melting eutectics. It is noteworthy that the extent of solute partitioning also depends on the extent of back diffusion and undercooling. The eutectic reactions increase weld cracking tendencies. However, reduced cooling rates also lead to low thermal stresses in the weldment. Therefore, in the present work, the reduced cracking tendency may attributed to reduced stress levels in the slowly cooled welds.

Fusion Zone Grain Structure

It is well known that the fusion-zone grain structure is controlled by the base metal grain structure and welding conditions. Initial solidification starts epitaxially on partially melted grains in the base metal. For cubic metals such as the nickel-base superalloys, the easy growth directions are the <100> directions. Conditions for growth are optimum when one of the easy growth directions coincides with the heat flow direction. The situation for the welds of single crystal is further simplified by the fact that multiple grain orientations are not available. Therefore, the epitaxial growth of dendrites at the fusion boundaries is on a single crystallographic orientation. The specific active dendrite orientation (among the six <100> easy growth directions) can be determined as a function of the solidification front orientation using a geometric model.[9,10]

A typical dendritic growth pattern in a transverse section of a PWA-1480 single-crystal EB weld made on the (001) plane along the [100] direction, at a speed of 12.6 mm s^{-1}, is shown in Fig. 4(*a*). Various active dendrite-growth variants regions are marked in Fig. 4(*b*). A schematic of the predicted dendrite-growth pattern for a weld along the [100] direction on a (001) surface, corresponding to the condition in Fig. 4, is shown in Fig. 5. Although a generic weld-pool shape was assumed when modeling the dendrite-growth pattern in Fig. 5, in general, the dendrite-growth pattern agrees with the weld pattern in Fig. 4. For example, in Fig. 4, three dendrite-growth orientations, namely the [001] orientation (vertical), [010] (horizontal), and $[0\bar{1}0]$

(horizontal) orientations are evident. The locations of these variants match the locations predicted by Fig. 5.

However, there are regions marked as "s" in Fig. 4 where the dendrite growth is not along one of the base-metal <100> variants. In these regions, a new crystal orientation exists, hence, the new region is a new grain and is referred to as a "stray crystal".[9] These regions were found to be abundant (>50%) in some of the welds. The stray crystals tended to be more abundant at the top center of the weld, near the crown, rather than along the weld edges or the root of the weld. Moreover, no clear and direct correlation between stray-crystal formation and welding or preheating conditions was found for either EB or laser welds. These grains are also observed in single-crystal casting practices and are often called "spurious crystals".[11] Their presence indicates that the weld and the base metal no longer constitute a perfect single crystal. This needs further investigation. During welding Fe-Cr-Ni single crystals, the stray crystals were not observed.[10] However, on doping Fe-Cr-Ni welds with sulfur, stray crystals formed in these welds.[12] The mechanisms for the formation of stray crystals can be related to solidification conditions. However, the spatial variation of temperature gradient and growth velocity in the weld pool must be considered. Therefore, only a qualitative interpretation of the stray-crystal formation is discussed.

Pollack et al.[11] found that during casting the stray-crystal formation increased with the tendency for dendrite side-branching during solidification and at slower cooling rates. Therefore, they concluded that dendrite fragmentation was the main cause of stray crystal formation. However, in the welds, the stray-crystal formation was greatest at the crown of the weld, along the centerline, where the local cooling rate is highest, and not in the regions with the lowest cooling rates. At the crown of the weld, the temperature gradient (G) is minimum, the growth rate (R) is at a maximum, and G/R is a minimum. The stray-crystal formation can be interpreted based on the degree of constitutional supercooling (CS) that is present ahead of the dendrite tip. The CS is related to the conditions that lead to planar stability of the solidification front. A plane front is stable if the following condition is met:[9]

$$\frac{G_L}{R} \geq -\frac{m_L C^*_s (1-k)}{k D_L}, \qquad (1)$$

where G_L = thermal gradient in the liquid,

R = growth rate,

m_L = liquidus slope,

C_s^* = solid concentration at the solid/liquid interface,

k = partition coefficient,

D_L = diffusion coefficient in the liquid.

If equation 1 is not satisfied, then CS is present and plane-front solidification is not stable. As the degree of CS increases, the condition for nucleation of new grains ahead of the solidification front as well as the degree of dendrite branching will increase. Thus, the tendency for stray-crystal formation is expected to increase as the degree of CS increases (i.e., as G/R decreases). In the case of the PWA-1480 nickel-base superalloy, the degree of partitioning is significantly greater and the solidification temperature range and tendency for stray-crystal formation are, therefore, also going to be large. At the centerline, because the G/R ratio is smaller compared with the sides of the weld, the probability of stray-crystal formation is high. In addition, one has to consider the effects of convection also on the dendrite fragmentation and its subsequent growth in front of the solid-liquid interface. Detailed correlation between local cooling rates, solute partitioning, and convection in the liquid on stray crystal formation need to be described in future.

The microstructural observations indicate that the cracks are often associated with stray-crystal formation. Therefore, it is highly desirable to reduce the occurrence of these stray crystals. Because there are only a few of these grains, the total high-angle grain boundary area is small. In the presence of low-melting eutectic liquid during solidification and, such a small high-angle grain boundary area, the extent of grain boundary wetting will be large. Therefore, the tendency to form cracks is enhanced in the presence of stresses. On the contrary, having more of these stray crystals may eliminate cracking by increasing the total grain boundary area and reducing the effective wetting.[3] However, this would defeat the purpose of the single crystallinity of the weld.

Microstructure Development

In addition to weld cracking, the final weld microstructure also governs the weld properties. The single-crystal nickel-base superalloy base metal is often heat treated to attain particular microstructural characteristics, such as the volume fraction of γ' and the composition of γ and γ' phases. However, during welding, the weld experiences melting, solidification, and subsequent cooling. The weld solidification will lead to eutectic reactions in the interdendritic regions. The continuous cooling of the weld will also lead to nonisothermal decomposition of γ to γ′ precipitates. Therefore, the weld microstructure is expected to be different from that of the base metal.

A typical microstructure of a PWA-1480 EB weld, with 500°C preheating, is shown in Fig. 6.[13] The microstructure shows an interdendritic boundary and the presence of cuboidal γ′ precipitates within the dendrites. In addition, wavelength dispersive X-ray (WDX) and energy dispersive X-ray (EDX) analyses of the dendrites showed elemental variation across the dendrites.[3] The analyses indicated that the dendrite core is depleted in tantalum and is enriched in tungsten. The dendrite core was also slightly depleted in titanium and aluminum. The preceding tendency is in agreement with published results of solidification partitioning coefficients.[14] This partitioning of elements into the liquid will lead to eutectic reactions during the final stages of solidification.[13] In agreement with this conclusion, the microstructure in Fig. 6 shows the presence of eutectic γ′ along the dendritic boundary. In addition, some amount of Laves phase was also found along the interdendritic regions.[9] It is known that the presence of such a eutectic microstructure at the interdendritic boundary will promote weld cracking and is not desirable.

It is speculated that rapid weld cooling conditions may lead to atomic-scale segregation of various elements at γ/γ′ interfaces and nonequilibrium compositions of γ and γ′ phases.[13] However, the field-ion microscopy (FIM) [see Fig. 7(*a*)] failed to show any interfacial segregation. If there were segregation of elements, FIM would have detected the decoration of these atoms along the interface. The compositions of γ and γ′ [see Fig. 7(b)] were found to be similar to that of base-metal values.[15] The composition profile showed the absence of segregation and also suggested that the concentration variations within γ and γ′ phases were not significant. This showed that in spite of continuous cooling conditions, the decomposition of γ to γ′ appears to have occurred in a fashion similar to that after standard heat treatments.

In the case of the CMSX-4 alloy, welded with a pulsed laser and without preheating, an interesting microstructure was observed (Fig. 8a).[16] The microstructure shows interdendritic boundaries with negligible amounts of eutectic products. Qualitative analysis indicated no significant elemental variation within the dendrites. The absence of a eutectic microstructure is attributed to the rapid solidification conditions attained in pulsed laser welds. The rapid solidification condition may lead to negligible partitioning or nonequilibrium solidification partitioning.[16] This, in turn, may lead to minimal enrichment of the last-solidifying liquid and therefore less chance of a eutectic reaction. In addition, the γ′ precipitate shapes were found to be irregular within the dendrites (Fig. 8b); this could be attributed to rapid weld cooling conditions as well. The faster cooling conditions might have led to solid-state decomposition of γ to γ' at large undercooling. However, this would also lead to nonequilibrium elemental partitioning between γ and γ' phases. In agreement with the previous hypotheses, the APFIM analysis [see Fig. 9(*a*) and (*b*)] of these welds showed extensive diffusion gradients of aluminum and chromium and the composition of the γ and γ' phases were different from that of the base metal.[17] In addition, the lattice misfit of γ and γ', based on the preceding information, was found to be positive compared to a negative value for the base metal. This may lead to lattice strains that in turn may induce changes in the γ' phase morphology.

In summary, the preceding experimental observations reiterate the complex interactions of thermal, mechanical, and metallurgical parameters and their effects on the final quality of the single-crystal nickel-base superalloy welds. Therefore, successful selection and design of the welding process and process parameters should consider the interactions that affect cracking, grain development, eutectic formation, and solid-state decomposition. Numerical models that can deal with thermo mechanical-metallurgical factors are necessary.

Numerical Modeling

At present there are no coupled models that can deal with the all of the phenomena previously described. However, there are individual models that can deal with the preceding processes in isolation. These models are reviewed in this section.

Models for Weld Cracking

Weld cracking results from the competition between the material resistance to cracking and the mechanical driving force for cracking during weld cooling.[8] The material resistance to weld cracking depends on the nonequilibrium nature of solidification, the presence of low-melting eutectic films, and the grain structure. The mechanical driving force is related to the local stress/-strain development at the trailing edge of the weld pool. Therefore, to model the weld cracking, thermomechanical effects along with the metallurgical factors should be considered. However, comprehensive models that can describe both mechanical and metallurgical parameters are not available. Recent work by Feng et al.[8] on local stress-strain conditions, based on macroscopic continuum mechanics, have provided valuable insight into the mechanical driving force for cracking.

Feng et al.[8] applied computational models to describe the mechanical driving force for weld cracking in nickel-base superalloy thin sheets. In this work, the development of transverse and longitudinal stresses at the weld centerline was calculated as a function of weld cooling. Figure 10 shows the stress development in a thin sheet of M738 nickel-base superalloy sheet as a function of temperature and various positions along the weld centerline. The calculations are for a free standing sheet of M738 alloy 50 × 50 mm in size and with a welding speed of 14.8 mm s^{-1}. In this analysis, cracking at a position will be promoted if a weak microstructure and/or a tensile stress exists. A transverse tensile stress will lead to longitudinal weld centerline cracking. Similarly, a longitudinal tensile stress will lead to transverse weld cracking.

Figure 10 plot shows iso-stress levels in different locations along the weld centerline as a function of temperature. The plots show that, initially, all the positions develop a compressive stress (transverse and longitudinal) behind the trailing edge of the weld pool (at temperatures below 1600 K). However, as the weld cools there is a transition from compressive to tensile stress. The transition for transverse stress [see Fig. 10(*b*)] to go from compressive to tensile, at the weld start, defines the critical temperature (at around 1550 K). Therefore, there is a high probability of longitudinal weld centerline cracking in these welds. In addition, the calculations also show the presence of a longitudinal tensile stress in the temperature range of 1400 to 1300 K [see Fig. 10(*c*)] in all the locations along the weld centerline. Because this alloy does form a low-melting-point eutectic, the probability of transverse cracks is also significant.

The previous calculations were found to agree with the experimental observations. For example, the model predicted the possibility of transverse cracks for the experimental conditions used when directly monitoring the surface during welding (see the section on direct observation of weld cracking). Moreover, Feng et al.[8] also showed a variation of this cracking tendency with the application of prestress on the weld specimens. This work gave crucial insight into local stresses that develop as a function of weld cooling. However, further work is necessary to couple these calculations with the metallurgical susceptibility for cracking.

The weld cracking in the mushy liquid-solid mixture zone in the presence of a tensile stress needs to be quantified. For example, it is known that large fractions of liquid do not always lead to weld cracks in the presence of small tensile stress-strain. Instead, the liquid film can heal the cracks by capillary action. However, the presence of a small amount of liquid film may promote the microcracks by rupture and subsequent interconnection of small microcracks. Moreover, the influence of weld grain development on the cracking (the effect of stray crystals compared to branched dendritic structure) is still unclear Finally, the presence of a low-melting eutectic film is related to the weld solidification rates. Future work should focus on this most needed estimation of metallurgical cracking susceptibility as a function of composition, weld cooling, and stress state.

Modeling Solidification Grain Development

The experimental data show that the cracking tendency in single crystals is related to the solidification grain structure development. Although, most of the grain structure development can be estimated using the geometric model,[10] further improvement is necessary. The geometric model for grain development should be coupled with weld thermal models.[18] The thermal models can estimate the weld pool geometry, temperature gradient, and growth velocities to a greater accuracy. These estimates can then be used to describe the most favored dendritic growth orientation as a function of spatial location. This coupled model may also allow one to estimate the G/R ratios and thereby calculate the probability for stray crystal formation.

Modeling Microstructure Development

In addition to the grain development, it is necessary to consider the formation of eutectic products. The presence of eutectic products in PWA-1480 EB welds and the absence of the same in CMSX-4 laser welds indicate that the eutectic reaction depends on both the cooling rates and the composition. Composition dependence of eutectic reactions in nickel-base superalloy can be estimated with software like ThermoCalc.[19] However, the cooling rate dependency must be estimated based on both thermodynamics and kinetics of solidification. The kinetics will decide the solute enrichment in the liquid as a function of solidification. The preceding dependency in a Ni-Al-Cr system was demonstrated with the coupled thermodynamic-kinetic software, DicTra.[20]

The solidification behavior in an alloy of Ni-20%Al-5%Cr (at.%) was simulated for two different cooling rates from 1700 K (10 and 100°C s^{-1}) using the DicTra software. In this simulation, an interdendritic spacing of 2 μm was chosen. The calculated volume percent of γ and liquid is plotted as a function of weld cooling time (Fig. 11). While cooling at 10°Cs^{-1}, the primary γ forms at ~5 s and then grows into the liquid. After 90% solidification, the calculations indicated the formation of eutectic γ' from the remaining liquid; this is because the liquid composition is enriched in aluminum. However, in the case of fast cooling, although the formation of primary γ is similar to the slow cooling rate, there is no indication of eutectic γ' formation. The solidification leads to 100% γ phase. The preceding calculations qualitatively support the microstructure development in PWA-1480 EB welds and CMSX-4 pulsed laser welds. However, these calculations have to be extended to multicomponent equilibrium[21] using better estimates of cooling rates in these welds.

In addition, the DicTra software can be used for simulating the solid state decomposition of γ into γ phase. An illustrative calculation was performed again with Ni-20%Al-5%Cr (at.%) in a system

2 μm in size. The simulation was performed for cooling rates of 10 and 100°C s^{-1}, after the solidification event described in Fig. 11. The compositional profiles of aluminum and chromium in γ and γ' phase are plotted for both cooling rates in Fig. 12. In the case of the 10°C s^{-1} cooling rate, the calculations showed the diffusional growth of eutectic γ' phase into the γ phase [see Fig. 12(*a*)]. In contrast, the calculations showed the nucleation and diffusional growth of γ' phase from completely solidified γ phase for a 100°C s^{-1} cooling rate [see Fig. 12(*b*)]. In these calculations, the diffusion in γ' was not considered. The plots in Fig. 12 show the movement of the γ/γ' interface to the left as a function of time. The plots for the high cooling rates show a presence of a large diffusion gradient in the γ phase compared to that of slow cooling rates. These results also qualitatively support the partitioning characteristics in PWA-1480 EB welds and CMSX-4 pulsed laser welds. However, the preceding calculations have to be extended to multicomponent equilibrium[21] and must be modified to consider the diffusion in the γ' phase.

Future Directions

Although separate models exist to describe the mechanical driving force for cracking, grain development, and microstructure development in single-crystal nickel-base superalloy welds, a coupled model that describes all of these phenomena during a typical thermal cycle needs to be developed. The failure criteria for weld cracking also need to be developed. The phase equilibria and kinetics in multicomponent nickel-base superalloy systems need to be integrated into the model and must be evaluated over a wide range of cooling conditions. In addition, the possibility of partitionless solidification during rapid solidification should be incorporated into these coupled models.

Summary and Conclusions

An overview of the most important physical processes in the welding of single-crystal nickel-base superalloys is presented. The experimental observation of weld cracking, solidification grain development, eutectic formation and solid state decomposition in these alloys illustrates the complex interplay of thermomechanical-metallurgical parameters. The formation of subsolidus weld cracking was observed directly. Weld cracking in nickel-base superalloys was attributed to the local stress-strain conditions, stray crystal formation, and the presence of low-melting eutectic films. The presence of stray crystals is attributed to the constitutional supercooling effect. The extent of the eutectic reaction was related to the cooling rate. The elemental partitioning between γ/γ' was found to depend on the weld cooling rate. Various modeling tools are available to describe these physical processes to a certain extent. However, these models need to be modified and integrated to describe the overall weldability and microstructural evolution during welding of nickel-base superalloy single-crystal welds.

Acknowledgments

The authors thank Dr. Z. Feng of EWI for providing the data on the local stress development, Mr. R. W. Reed of ORNL for production of single-crystal welds, Dr. M. K. Miller of ORNL for the help in APFIM work, Dr. R. P. Schaefer of United Technologies, Inc. for providing PWA-1480, and Dr. M. Burke of Westinghouse Electric Corporation Inc. for providing CMSX-4 alloys. The authors also thank Drs. S. Viswanatahn and R. Subramanian for helpful comments on the paper. This research is sponsored by the Division of Materials Sciences, U.S. Department of Energy, under contract DE-AC05-96OR22464 with Lockheed Martin Energy Research Corporation.

References

1. M. Gell and D. N. Duhl: 'Advanced high temperature alloys,' 41-49; 1985, Materials Park, OH, ASM.
2. K. Harris, G. L. Erickson, S. L. Sikkenga, W. D. Brentnall, J. M. Aurrecochea, and K. G. Kubarych: 'Superalloys 1992,' S. D. Antolvich, R. W. Stusrud, R. A. MacKay, D. L. Anton, T. Khan, R. D, Kissinger, and D. L. Klarstrom, eds., 297-306, 1992.
3. S. A. David, J. M. Vitek, S. S. Babu, L. A. Boatner, and R. W. Reed: 'Welding of nickel base superalloy single crystals,' *Science and Technology of Welding and Joining*, 1997, **2**, 79-88.
4. C. S. Smith: *Trans. Am. Inst. Min. Metall. Eng.*, 1948, **175**, 15-51.
5. *LaserStrobe camera system*, Control Vision Inc., Idaho Falls, ID 83405.
6. G. M. Goodwin: 'Development of a new hot-cracking test - The SigmaJig,' *Welding Journal*, 1987, **66**, 33s-38s.
7. M. K. Miller: *J. Phys.*, 1986, **C47**, 493.
8. Z. Feng, S. A. David, T. Zacharia, and C. L. Tsai: 'Quantification of thermomechanical conditions for weld solidification cracking,' *Science and Technology of Welding and Joining*, 1997, **2**, 11-19.

9. J. M. Vitek, S. A. David, and L. A. Boatner: 'Microstructure development in single-crystal nickel-base superalloy welds,' *Science and Technology of Welding and Joining*, 1997, in press.

10. M. Rappaz, S. A. David, J. M. Vitek, and L. A. Boatner: 'Development of microstructures in Fe-15Ni-15Cr single crystal electron beam welds,' *Metall. Trans. A*, 1989, **20A**, 1125-1138.

11. T. M. Pollack, W. H. Murphy, E. H. Goldman, D. L. Uram, and J. S. Tu: in 'Superalloys 92,' S. D. Antolvich, R. W. Stusrud, R. A. MacKay, D. L. Anton, T, Khan, R, D, Kissinger and D. L. Klarstrom, eds., 125-134, 1992.

12. S. A. David and J. M. Vitek: 'Correlation between solidification parameters and weld microstructures,' *Inter. Meter. Rev.*, 1989, **34**, 213-245.

13. S. S. Babu, S. A. David, and M. K. Miller: *Applied Surface Science*, 1996, **94/95**, 280-287.

14. S. N. Tewari, M. Vijayakumar, J. E. Lee, and P. A. Currei: 'Solutal partition coefficients in nickel-based superalloy PWA-1480,' *Mater. Sci. Eng.*, 1991, **A141**, 97-102.

15. D. Blavette, P. Caron, and T. Khan, 'An atom probe investigation of the role of rhenium additions in improving creep resistance of Ni-base superalloys,' *Scripta. Met.*, 1986, **20**, 1395.

16. S. S. Babu, S. A. David, J. M. Vitek, and M. K. Miller: 'Atom probe field-ion microscopy investigation of CMSX-4 ni-base superalloy laser beam welds,' *Journal De Physique IV*, 1996, **C5**, 253-258.

17. H. Murakami, H. Harada, and H. K. D. H. Bhadeshia, 'The location of atoms in Re- and V-containing multicomponent nickel-base single-crystal superalloys,' *Appl. Surf. Sci.* 1994, **76/77**, 177-183.

18. K. Mundra, T. DebRoy, S. S. Babu, S. A. David: 'Weld metal microstructure calculations from the fundamentals of transport phenomena in the arc-welding of low-alloy steels,' *Welding Journal*, 1997, **76**, 163s-171s.

19. B. Sundman, B. Jansson, and J.-O. Andersson: 'The Thermo-calc database system,' *Calphad*, 1985, **9**, 153-190.

20. J.-O.Andersson, L. Höglund, B. Jönsson, and J. Ågren: 'An experimental and theoretical study of cementite dissolution in an Fe-Cr-C alloy,' *Metall Trans. A*, 1991, **22A**, 1745.

21. N. Saunders: in 'Superalloys 1996,' R. D. Kissinger, D. J. Deye, D. L. Anton, A. D. Cetel, M. V. Nathal, T. M. Pollack, and D. A. Woodford, eds., 101-110, 1996.

Table 1. Composition (at.%) of single-crystal nickel-base superalloys:

Alloy	Cr	Al	Co	Mo	W	Ti	Ta	Re	Hf
CMSX-4	7.5	12.7	9.9	0.38	2.1	1.3	2.2	0.95	0.034
PWA-1480	11.5	11.0	5.1	-	1.3	1.9	4.0	-	-

Balance is nickel.

Table 2. Effect of welding direction (alloy: PWA-1480, process: electron beam) on weld quality

Surface Orientation	Weld Direction	Welding Speed, mm s^{-1}	Weld Quality
(001)	[100]	4.2	Cracks
(001)	[110]	4.2	Cracks
(001)	[100]	42.0	Cracks
(001)	[110]	42.0	Cracks

Table 3. Effect of welding speed (alloy: PWA-1480, process: electron beam) and preheating (500°C) on weld quality

Surface Orientation	Weld Direction	Welding Speed, mm s^{-1}	Preheating Temperature	Weld Quality
(001)	[100]	4.2	RT	Cracks
(001)	[100]	8.4		Cracks
(001)	[100]	12.6		Cracks
(001)	[100]	16.8		Cracks
(001)	[100]	21.0		Cracks
(001)	[100]	25.2		Cracks
(001)	[100]	42.0		Cracks
(001)	[100]	4.2	500°C	No Cracks
(001)	[100]	6.3	500°C	No Cracks
(001)	[100]	42.0	500°C	Cracks

RT - room temperature

Table 4. Effect of pulse rate (alloy: PWA-1480, process: laser beam) on weld quality

Surface Orientation	Weld Direction	Welding Speed, mm s^{-1}	Number of pulses, s^{-1}	Preheating temperature	Weld Quality
(001)	[100]	12.6	30	RT	Cracks
(001)	[100]	12.6	40	RT	Cracks
(001)	[100]	12.6	60	RT	Cracks
(001)	[100]	12.6	100	RT	Cracks
(001)	[100]	12.6	150	RT	Cracks
(001)	[100]	12.6	200	500°C	Cracks
(001)	[100]	12.6	30	500°C	Cracks
(001)	[100]	12.6	40	500°C	Cracks
(001)	[100]	12.6	60	500°C	Cracks
(001)	[100]	12.6	100	500°C	Cracks
(001)	[100]	12.6	150	500°C	Cracks
(001)	[100]	12.6	200	500°C	Cracks
(001)	[100]	4.2	100	500°C	No Cracks
(001)	[100]	2.1	100	500°C	No Cracks

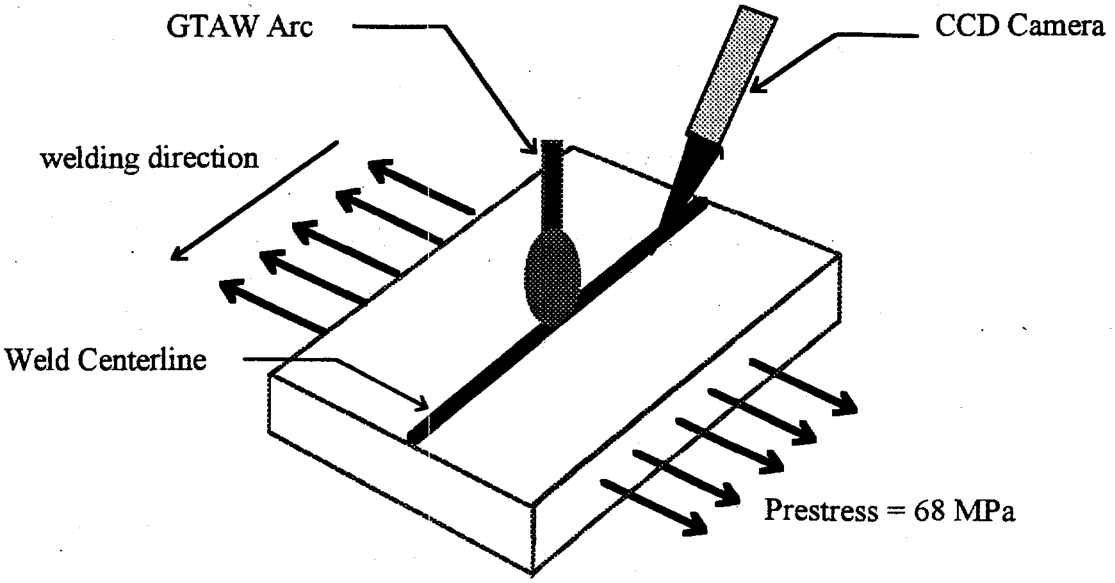

Fig. 1. Schematic setup for studying weld cracking dynamics in the vision-systems. The welding was performed in a SigmaJig fixture (not shown in the figure).

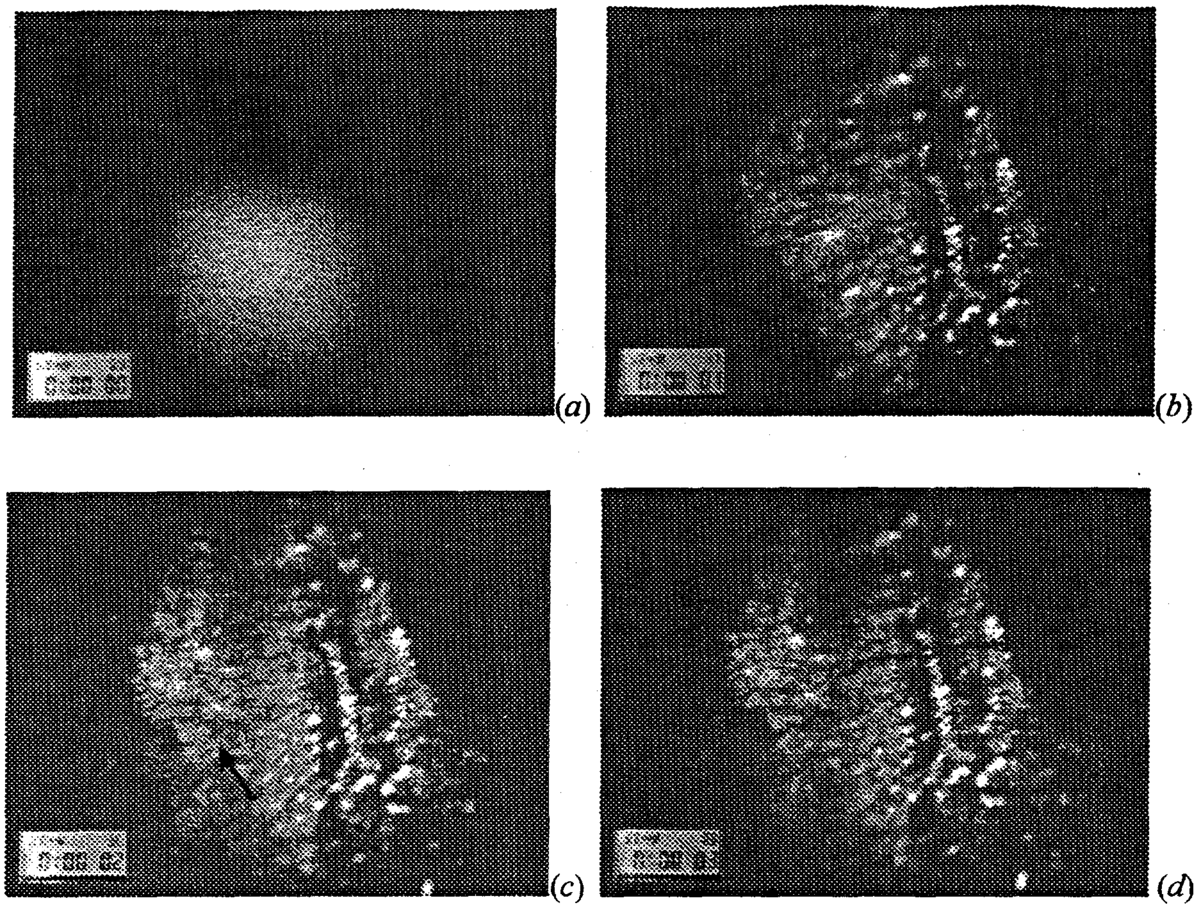

Fig. 2. Evolution of weld cracks in an experimental nickel-base superalloy recorded by a vision-system: (*a*) the passage of arc under the camera at 0.09 seconds; (*b*) weld solidification complete at 01.19 seconds; (*c*) 2.30 seconds (arrow marks the formation of a transverse crack); and (*d*) 03.06 seconds (cracked weld).

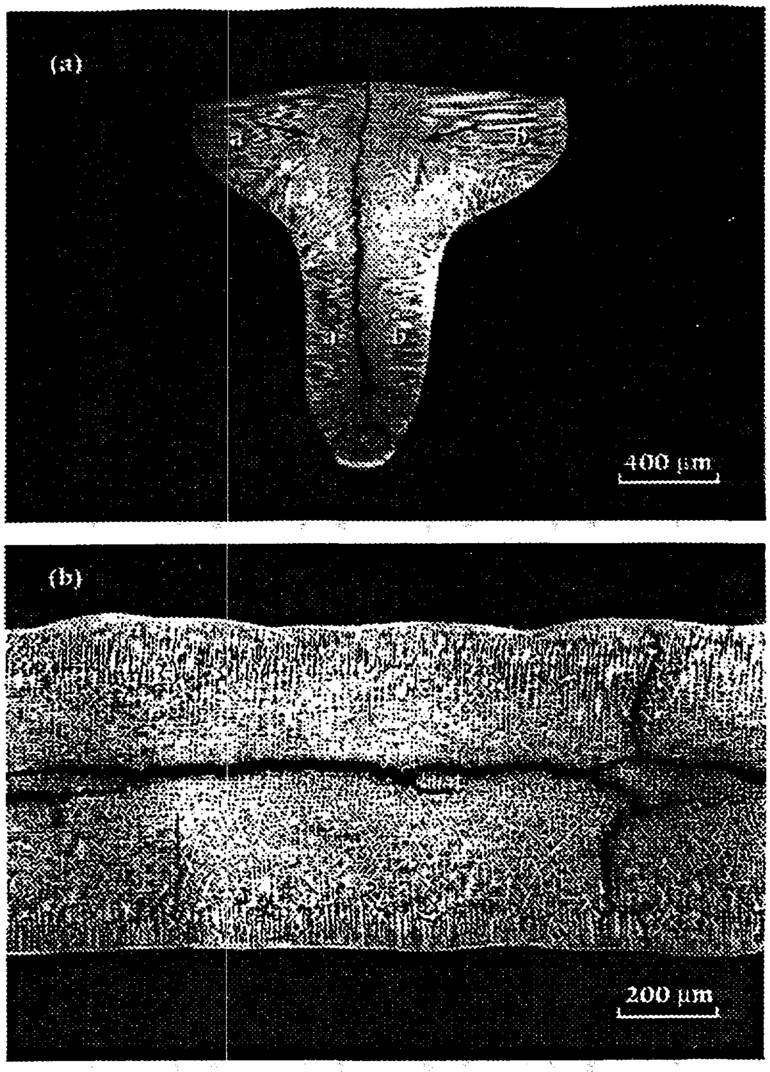

Fig. 3. Optical microstructure of electron beam weld (12.6 mm s^{-1}) PWA-1480 alloy single-crystal with both longitudinal and transverse cracks. (a) Transverse macroscopic view and (b) top surface view. The regions marked as "a" and "b" in Fig. 3(*a*) consist of dendrites that grow epitaxially, and the regions marked by arrows consist of stray crystals.

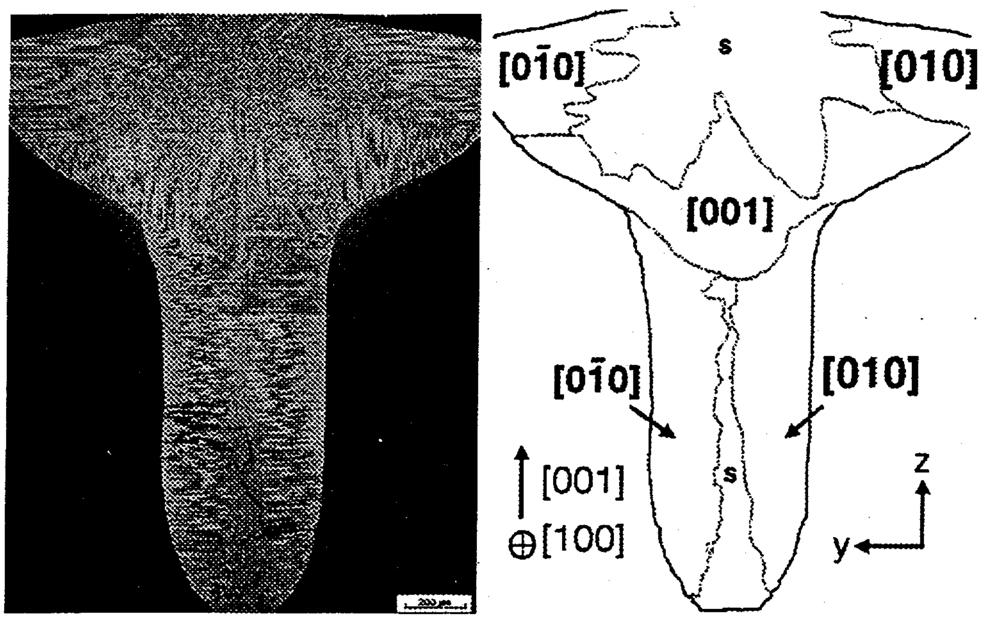

Fig. 4 Optical microstructure of dendritic patterns in a PWA-1480 single-crystal electron beam weld. The microstructure shows three variants of dendrite-growth directions. The figure on the right side shows the classification of various growth directions in the weld.

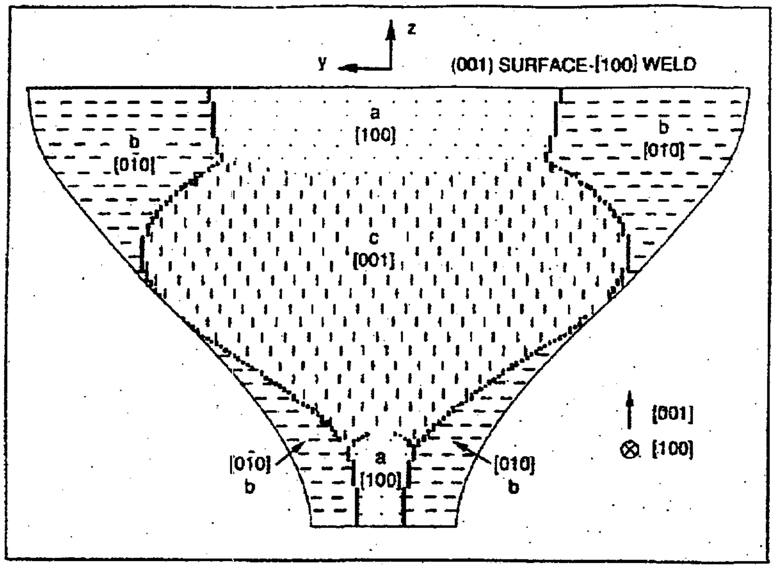

Fig. 5 Schematic diagram of the expected dendritic-growth zones for the same sample and the weld orientation shown in Figure 4. A generic weld-pool shape was assumed that was somewhat different from the actual pool shape in Figure 4.

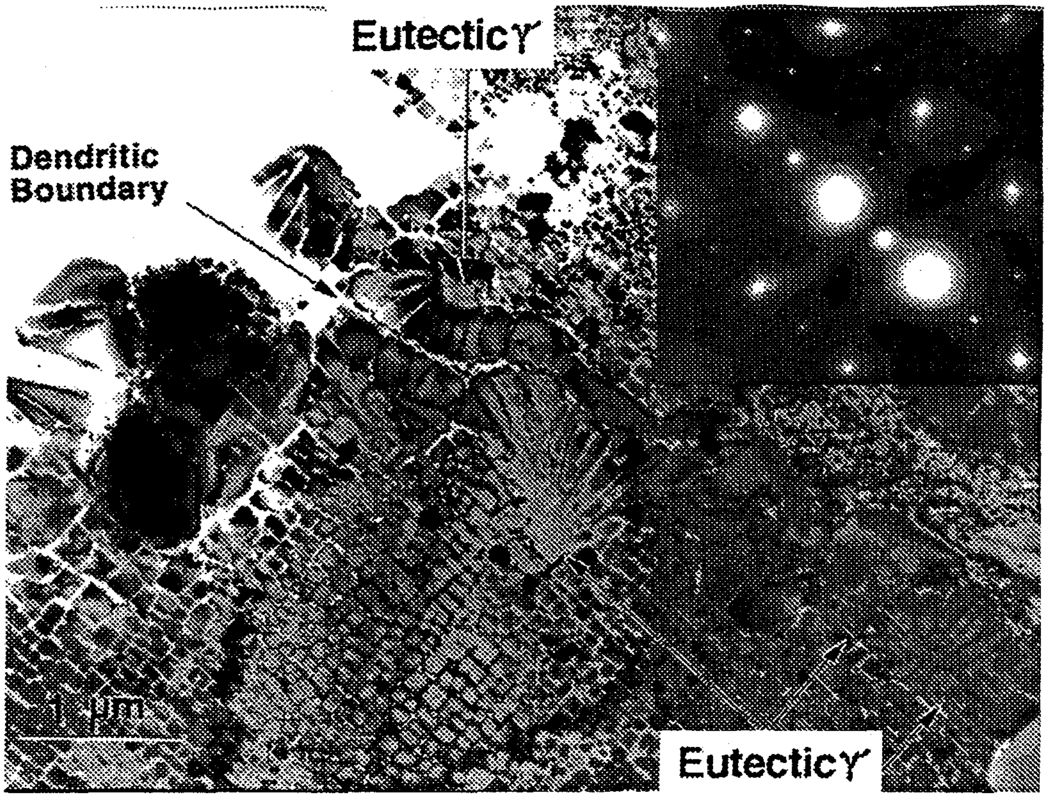

Fig. 6 Transmission electron micrograph of the weld metal region of a PWA-1480 electron beam weld (4.2 mm s^{-1}) in the as-welded condition. The microstructure shows an interdendritic boundary decorated with eutectic γ′ precipitates (marked by arrows). The electron diffraction is taken near the [001] zone and is consistent with the presence of γ′.

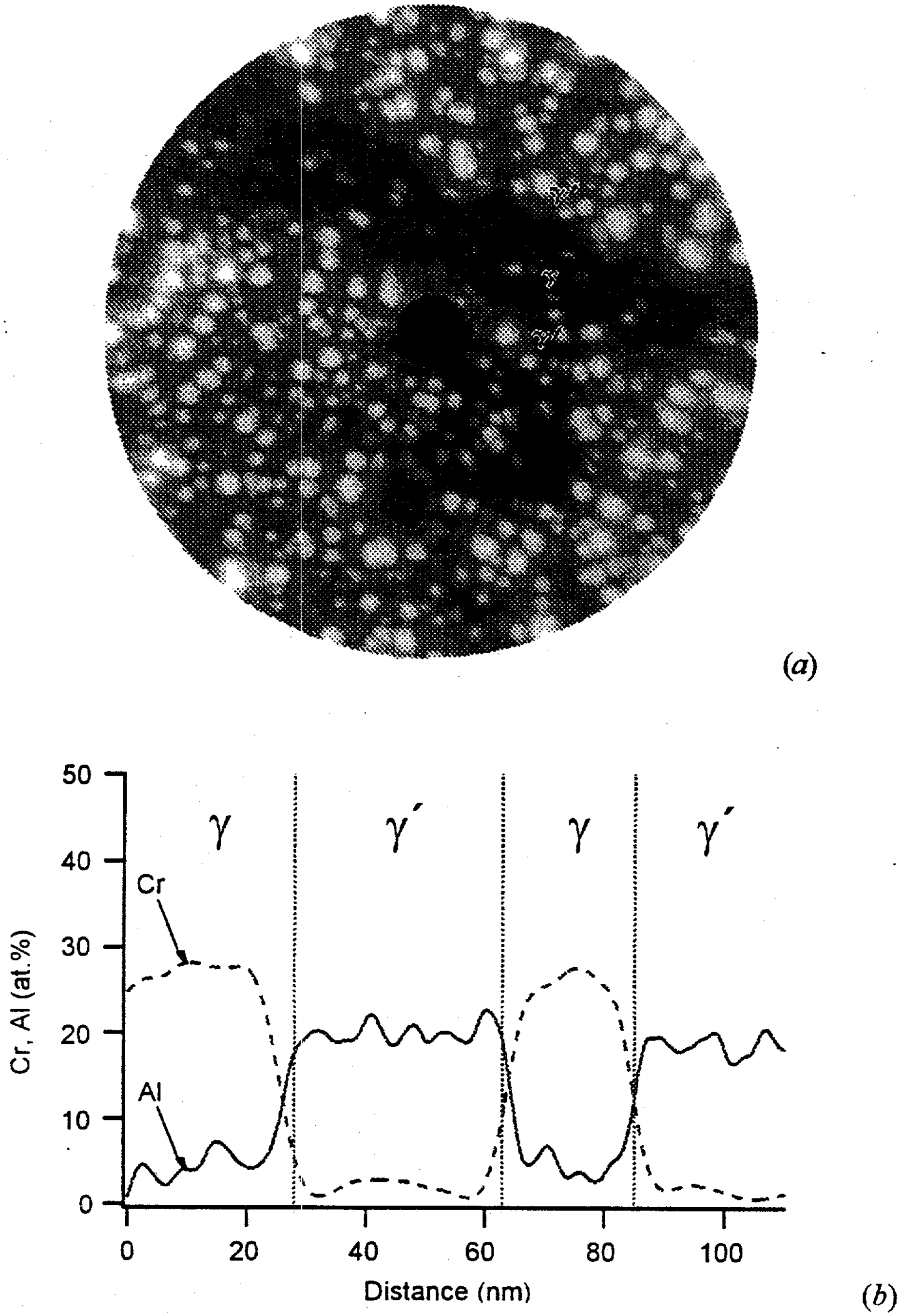

Fig. 7 (*a*) Field-ion micrograph of γ/γ′ interface in a PWA-1480 electron beam weld. The FIM micrograph showed the absence of interfacial segregation. (*b*) APFIM concentration profile of aluminum and chromium and shows negligible concentration gradients within γ or γ′ phases.

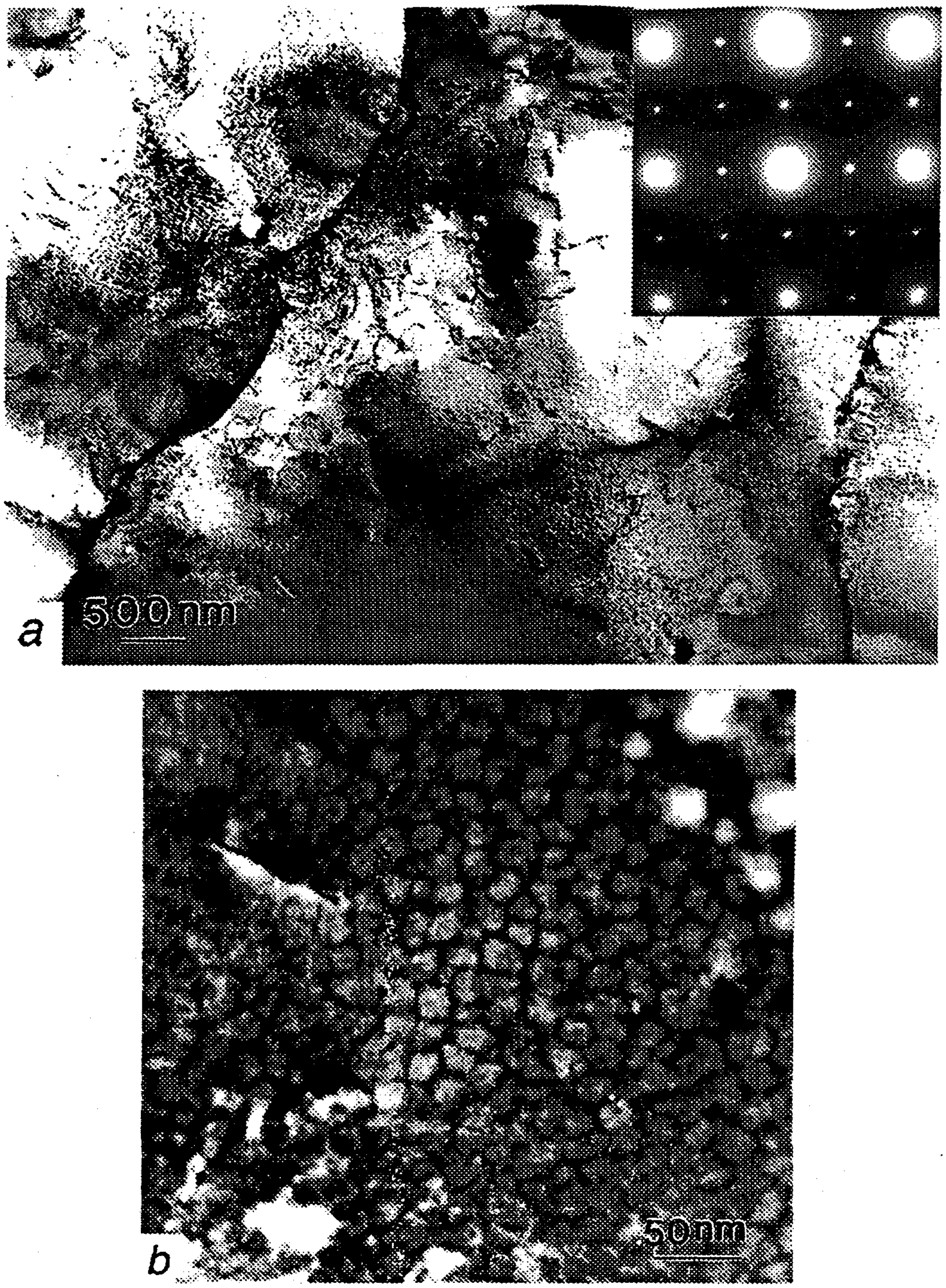

Fig. 8 (*a*) Low-magnification micrograph of a CMSX-4 pulsed laser weld showing interdendritic boundaries with negligible eutectic γ' precipitates. The electron diffraction confirmed the presence of γ' within the dendrite. (*b*) Higher-magnification micrograph illustrating the irregularly shaped and fine γ' precipitates.

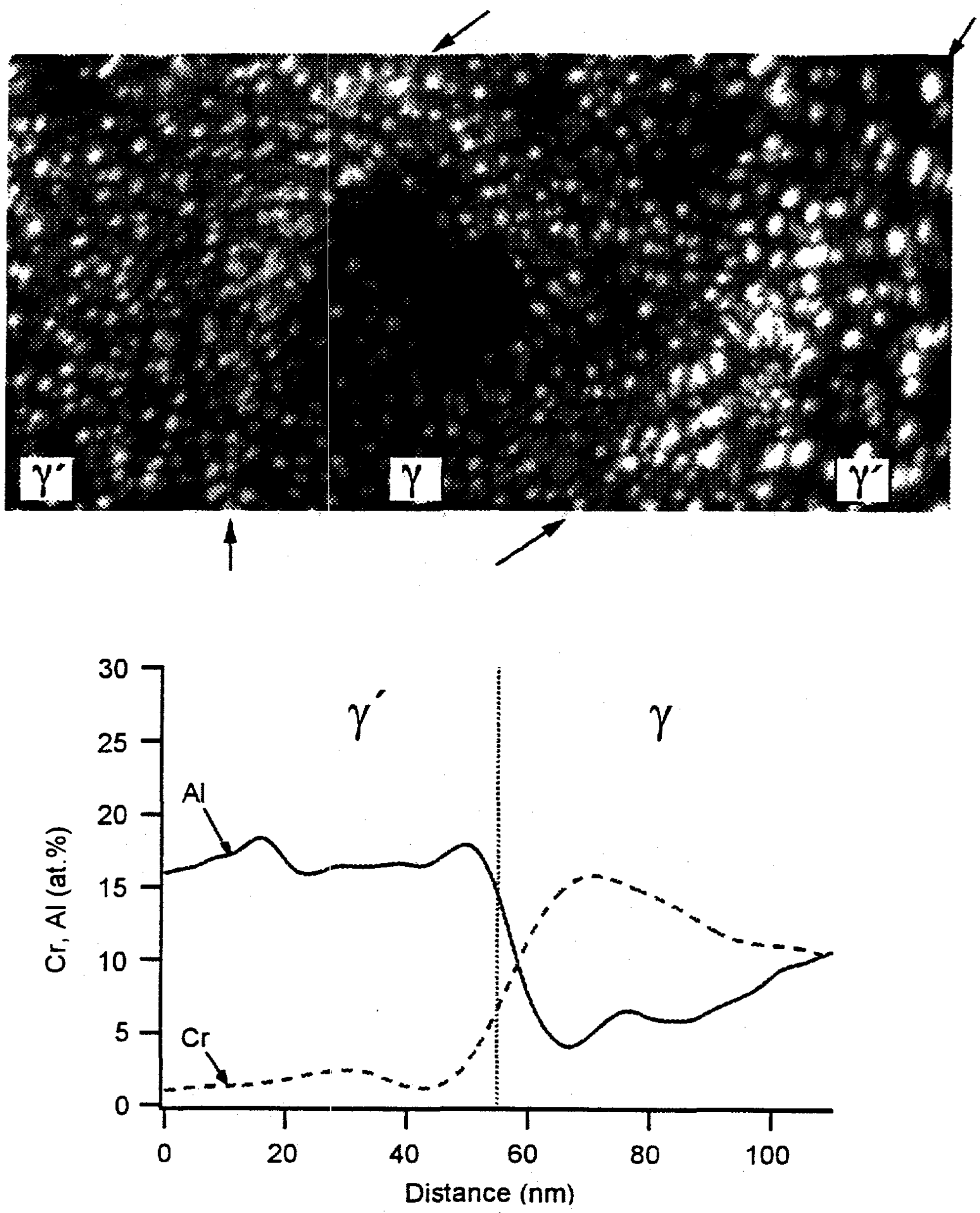

Fig. 9. (*a*) Field-ion micrograph of γ/γ' interface in a CMSX-4 pulsed laser beam weld. (*b*) APFIM concentration profile of aluminum and chromium and showed large concentration gradients within the γ phase.

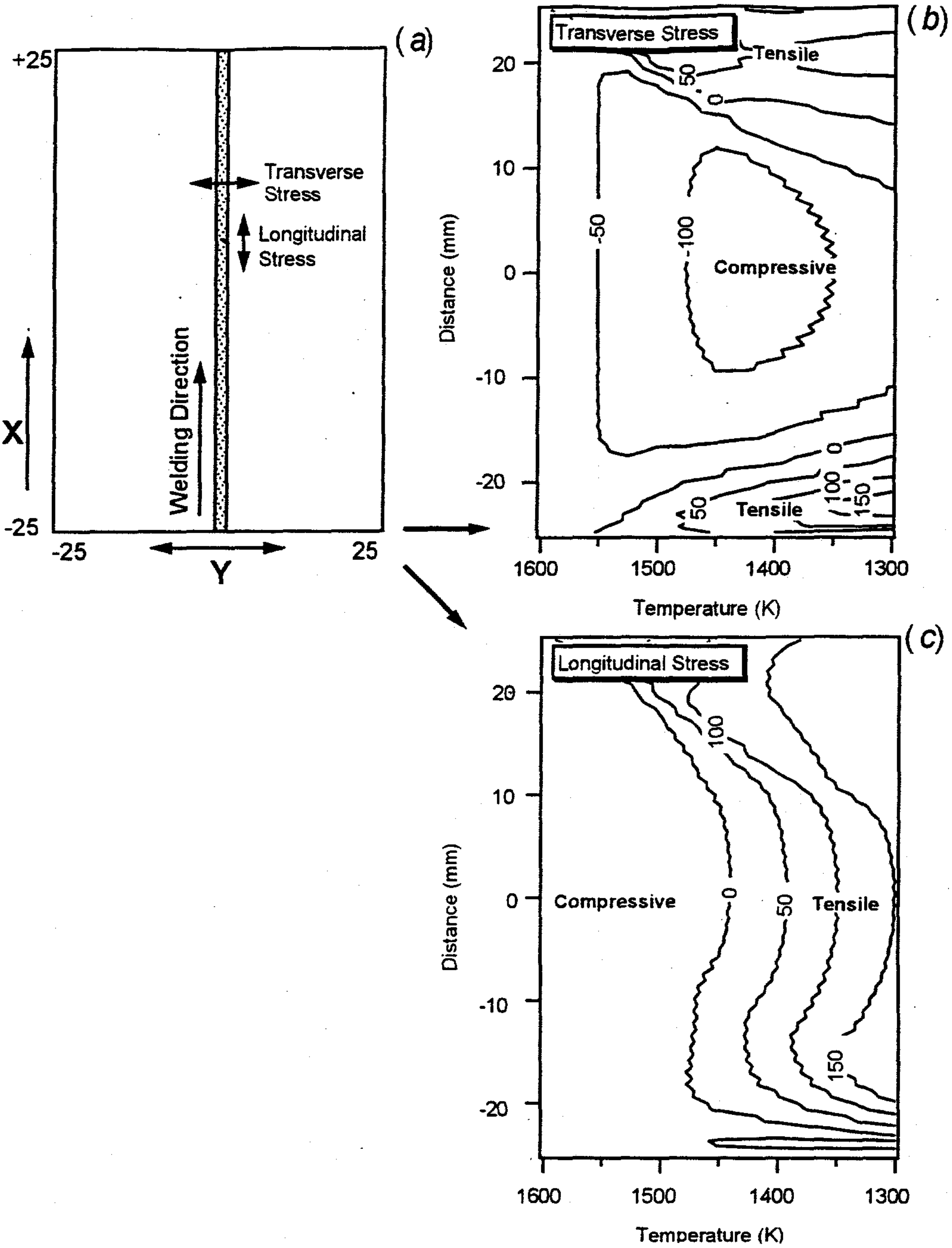

Fig. 10 (*a*) Schematic illustration of the specimen, welding direction, and the directions of stress. Stress development in the weld is calculated as a function of distance (along X direction) at the weld centerline (Y=0) and temperature during weld cooling. Iso-stress contour plots of (*b*) transverse stress (MPa) and (*c*) longitudinal stress (MPa) as a function of distance from the weld start (X) and the temperature.

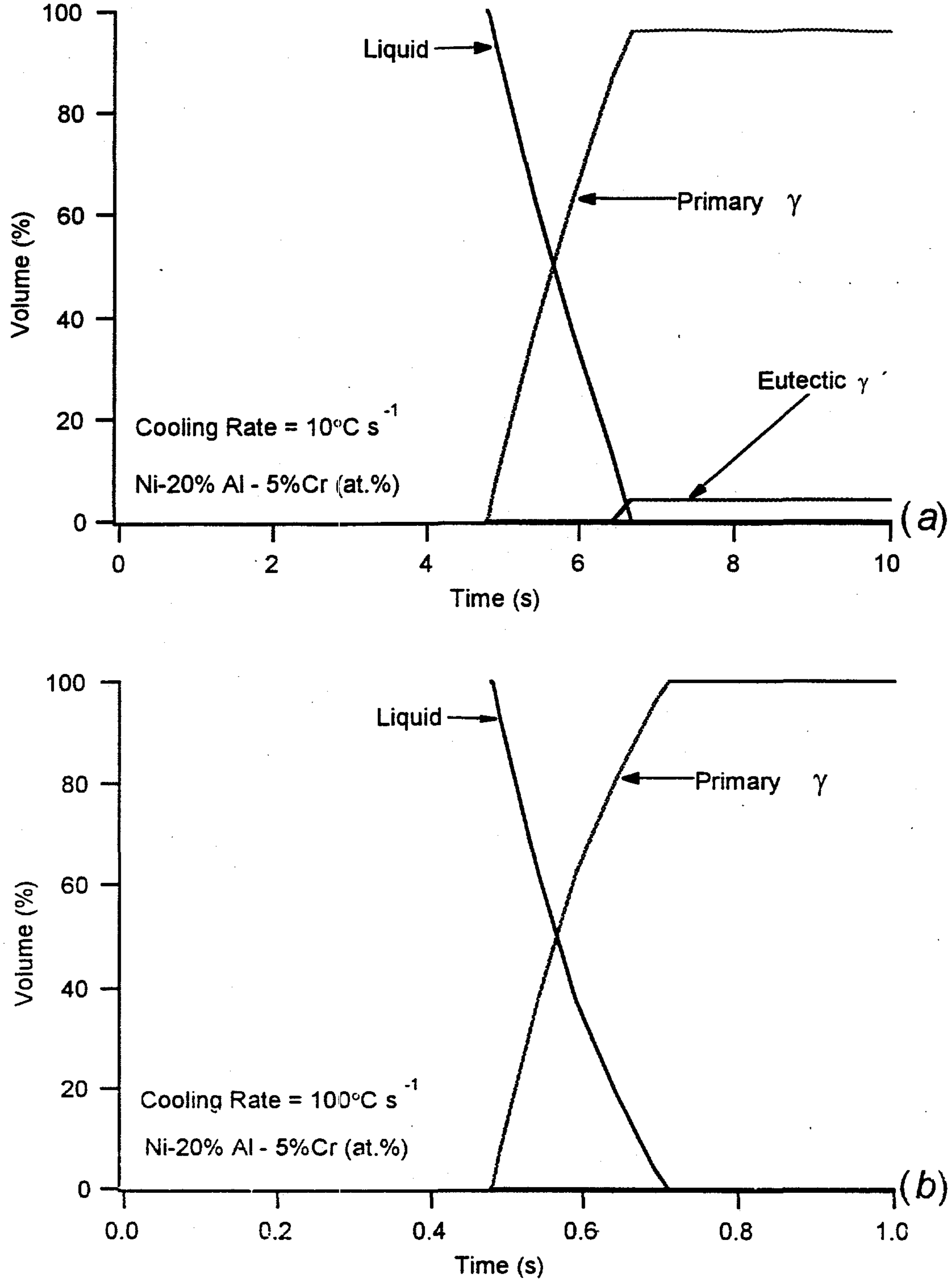

Fig. 11 Prediction variation of the amount of liquid, primary γ phase and eutectic γ′, as a function of time for two different cooling rates, that is at (*a*) 10°C s^{-1} and at (*b*) 100°C s^{-1} from 1700 K

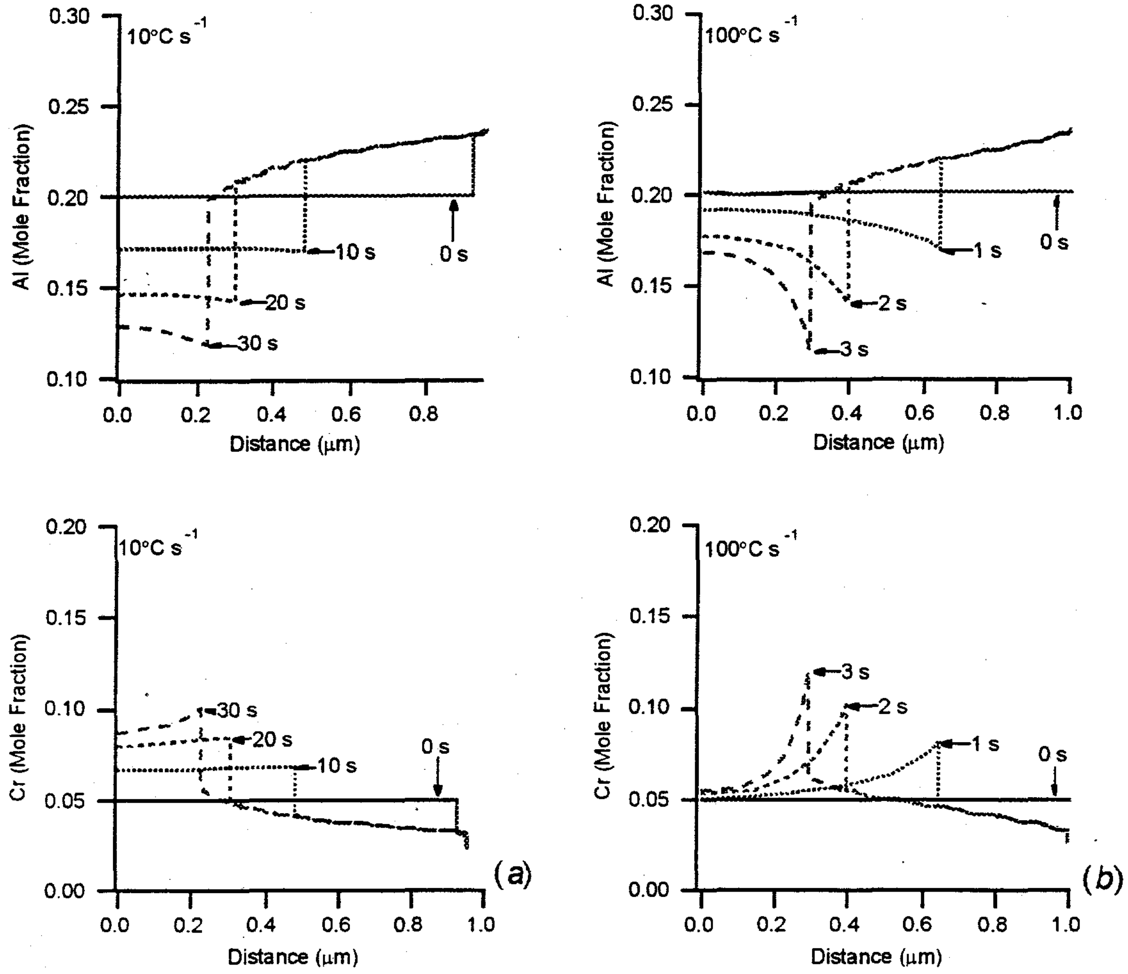

Fig. 12 Predicted concentration profiles of chromium and aluminum in the γ and γ' phases as a function of time for two different cooling rates, that is at (*a*) 10°C s^{-1} (the growth of eutectic γ' phase) and at (*b*) 100°C s^{-1} (nucleation and growth of γ' phase), after the completion of solidification at 1600 K.